Article

Journal of
Nanoscience and Nanotechnology
Vol. 19, 1–9, 2019
www.aspbs.com/jnn

Controlled Synthesis of Well-Aligned and Highly Ordered TiO_2 Nanotubes Without Bundling for Enhanced Solar-Powered Photoelectrochemical Responses

Chin Wei Lai[1,*], Kung Shiuh Lau[1], and Pui May Chou[2]

[1] *Nanotechnology and Catalysis Research Centre (NANOCAT), University of Malaya, 50603 Kuala Lumpur, Malaysia*
[2] *School of Engineering, Faculty of Built Environment, Engineering, Technology & Design, Taylor's University Lakeside Campus, No. 1, Jalan Taylor's, 47500 Subang Jaya, Selangor Darul Ehsan, Malaysia*

Using solar-powered water electrolysis systems for hydrogen generation is a key decision for the development of a sustainable hydrogen economy. A facile approach is presented in the present investigation to improve the solar-powered photoelectrochemical performance of water electrolysis systems by synthesising well-aligned and highly ordered TiO_2 nanotube films without bundling through the electrochemical anodisation technique. Herein, geometrical calculations were conducted for all synthesised TiO_2 nanotubes, and determination of the aspect ratio (*AR*) and geometric surface area factor (*G*) was achieved. On the basis of the collected data, well-aligned TiO_2 nanotubes with an *AR* of approximately 60 and *G* of approximately 400 $m^2 \cdot g^{-1}$ were successfully formed in an electrolyte mixture of ethylene glycol with 0.3 wt% NH_4F and 5 wt% H_2O_2 at 40 V for 60 min. The nanotubes were subsequently annealed at 400 °C to form anatase-phase TiO_2 nanotube films. The resultant well-aligned and highly ordered TiO_2 nanotube films exhibited a photocurrent density of 1.5 $mA \cdot cm^{-2}$ due to a large number of photo-induced electrons moving along the tube axis and perpendicular to the Ti substrate, which greatly reduces interfacial recombination losses.

Keywords: Hydrogen, Titanium Dioxide, Electrochemical Anodisation, Aspect Ratio, Geometric Surface Area Factor.

1. INTRODUCTION

At present, solar-powered water electrolysis systems for hydrogen generation are the most flexible and tenable solution for storing renewable energy on a large, long-term scale. Theoretically, the solar-powered photoelectrochemical response for hydrogen generation requires three basic characteristics: (a) high stability against photocorrosion in aqueous solution, (b) visible light photosensitivity with low recombination charge carrier losses and (c) a metal oxide semiconductor film with a conduction band that is more electronegative than that of the hydrogen production level (O_2/H_2O).[1–4] Several metal oxide semiconductor candidates have been investigated and studied to meet the basic characteristics of a solar-powered photoelectrochemical system. Unfortunately, high photostability and efficient visible light harvesting from solar energy coupled with a favourable metal oxide semiconductor-redox energetic have yet to be fully achieved. Some success has been obtained by applying metal oxide semiconductor films with a wide band gap energy, especially titanium dioxide (TiO_2) films.[5–8] TiO_2 provides unique electronic and functional properties compared with other metal oxide semiconductor materials, such as ZnO, ZnS and GaN. The main advantages of TiO_2 as a photoelectrode when applied to a solar-powered water electrolysis system include low production cost, non-toxicity, strong photocatalytic activity and exceptional photo-corrosion resistance in solution.[3–9] However, TiO_2 alone is impractical as a metal oxide semiconductor photoelectrode for solar-powered photoelectrochemical systems given its poor solar irradiation response on account of its large band gap energy (3.2 eV for the anatase polymorph and 3.0 eV for the rutile polymorph) and photogenerated electron–hole pair recombination, which is thermodynamically favourable.[3, 9–12] Because light-induced redox processes leading to the transfer of excited electrons to the conduction band of a

*Author to whom correspondence should be addressed.

metal oxide semiconductor are a surface phenomenon of selective oxidation and reduction processes, a large aspect ratio (*AR*) and geometric surface area factor (*G*) can be expected in the metal oxide semiconductor photoelectrode. Additional excited electrons can be triggered to flow toward the back contact of the photoelectrode and then move to the cathode to further reduce H^+ into hydrogen gas. Therefore, a 1D nanostructure, such as a well-aligned and highly ordered nanotubular structure, is inferred to enhance solar-powered photoelectrochemical processes substantially in metal oxide semiconductor films.[10, 12–13]

Oxidation and dissolution reactions during electrochemical anodisation remarkably influence the morphological and structural characteristics of 1D nanotubes and their properties. Although excess fluoride (F^-) can stimulate the growth rate of TiO_2 nanotubes to achieve the desired length, pore diameter and wall thickness, disequilibrium reactions between oxidation and dissolution remain must be addressed. To acquire the appropriate dimensions and morphologies of TiO_2 nanotube films for enhanced solar-powered photoelectrochemical performance, a controlled synthesis procedure for producing well-aligned and highly ordered TiO_2 nanotubes must be developed; such development, however, remains challenging. In general, highly ordered TiO_2 nanotube arrays exhibit undesirable bundling, which substantially reduces the photoelectrochemical performance of the system due to poor absorption of photons from solar irradiation into the inner portions of the tube structures. Thus, producing a highly efficient solar-powered water photoelectrochemical system including TiO_2 nanotubes without bundling problems as a photoelectrode is difficult unless the above-mentioned issues are addressed.

In our previous study, field-assisted oxidation, field-assisted dissolution and chemical dissolution were improved by $^{\cdot}OH$ and $HO_2^{\cdot}$ radicals when sufficient H_2O_2 was introduced to the electrolyte; such addition, in turn, promoted the growth of strong and bundle-free nanotubes on a Ti substrate,[17] and the resultant nanotubes had sufficient force to sustain the coefficients of thermal expansion and shrinkage that eventually lead to a peeling-off problem after drying. In the present investigation, the influence of adding H_2O_2 to ethylene glycol as an oxygen provider to supply sufficient amounts of O^{2-} to accelerate the anodic oxidation for growing highly ordered nanotube arrays was studied in detail. Geometrical calculations were used to obtain the aspect ratio (*AR*) and geometric surface area factor (*G*) of TiO_2 nanotubes, and the effects of anodisation time, anodisation potential and F^- content of the electrolyte on the surface morphology of the oxide layer on Ti foil were evaluated. This study demonstrates the validity of the proposed approach to determine the active surface area of highly ordered TiO_2 nanotube arrays by combining field-emission scanning electron microscopy (FESEM) with model calculations. The newly developed method utilised a rapid determination calculation to determine the geometric surface area.

2. EXPERIMENTAL DETAILS

In the present study, pure Ti foil (99.7% purity, 0.127 mm thickness; Sigma Aldrich) was selected as the substrate. The foil was cut into the desired dimensions of 50 mm × 10 mm and then degreased by sonication in acetone for 30 min using a Thermo-6D ultrasonic cleaner (40 kHz, 180 W). Next, the foils were dried in ambient temperature. The electrolyte composition plays a crucial role in determining the dimensions and morphologies of TiO_2 nanotubes synthesised via electrochemical anodisation. The structural morphology of the resulting nanostructure is either compact nanotubular or porous. Herein, ethylene glycol was used as the electrolyte. Prior to anodisation, 0.3 wt% NH_4F and 5 wt% H_2O_2 were dissolved in the electrolyte, and the mixed solution was stirred for 30 min via magnetic agitation to dissolve the solid reagents homogeneously.

For electrochemical anodisation, Ti foil (20 mm × 50 mm) was connected to the positive terminal of a DC power supply (CBS Scientific EPS-200X) as the anode in a two-electrode configuration. Pt foil (20 mm × 50 mm) was applied as the counter (cathode) electrode and connected to the negative terminal of the power supply. Subsequently, the foils were exposed to the prepared ethylene glycol electrolyte (100 ml), and the distance between the electrodes was fixed at ∼20 mm. Anodisation was carried out through manual switching of the power supply on and off. Monitoring of the exposure time at the desired potential was performed. The smooth transfer of air bubbles supplied from the bottom of the anodisation tanker at a flow rate of 600 ml min^{-1} helped homogenise the electrolyte and maintained a uniform current during electrochemical anodisation. Meanwhile, an air pump forced sufficient oxygen into the anodisation tank by increasing surface agitation. Upon completion of anodisation, the as-anodised TiO_2 foil was cleaned with deionised water and immersed in acetone for sonication (Thermo-6D ultrasonic cleaner, 40 kHz, 180 W) for 1 min to remove the remaining electrolyte on the surface of the foil and eliminate debris and precipitation layers on the surface of the formed nanostructures.[14] A schematic of the electrochemical anodisation set-up is shown in Figure 1.

Next, heat treatment of the as-anodised TiO_2 foils was conducted to convert amorphous TiO_2 structures into crystalline structures. Anatase TiO_2, which can be obtained by annealing at 400 °C for 4 h in an air atmosphere, is the most desirable structure of the compound. Based on our previous studies and investigations, complete transformation from amorphous TiO_2 into anatase crystalline TiO_2 could be achieved under the above conditions.[15] Annealing is crucial because anatase TiO_2 is a well-known

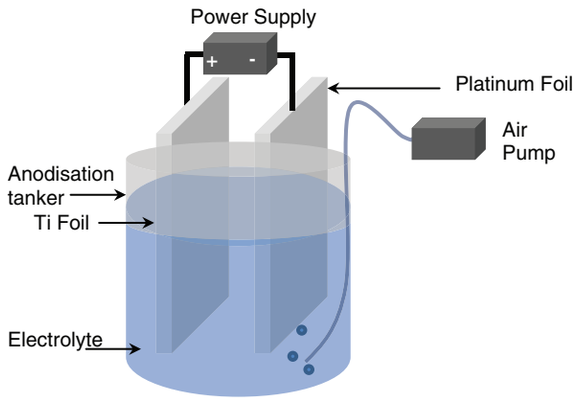

Figure 1. Schematic of the electrochemical anodisation set-up.

crystalline structure in solar-powered photoelectrochemical systems.[15–16] Herein, three stages of heat treatment were conducted, i.e., heating, soaking and cooling. Heating and cooling rates of 5 °C/min were applied during the annealing process, and the soaking time was fixed at 4 h.

The surface and cross-sectional morphologies of the anodised samples were observed via FESEM using a JEOL JSM 7600-F instrument operated at 5 kV with a working distance of approximately 1 mm. Then, phase determination of the anodised samples was performed by X-ray diffraction (XRD) using a Bruker AXS D8 Advance instrument with a Cu target (Ni filter) and Kα radiation ($\lambda = 0.1546$ nm) over the 2θ range of 20°–70°. The solar-powered water electrolysis characteristics of the anodised samples were characterised using a three-electrode cell under a 150 W Xe arc lamp with an intensity of 800 W/m^2 to produce a uniform spectrum across the entire UV-visible-infrared wavelength range. In this case, the anodised samples served as the working electrode, a Pt rod served as the counter electrode and Ag/AgCl in saturated KCl served as the reference electrode. The electrodes were dipped in an electrolyte of 1 M KOH aqueous solution and connected to a potentiostat (Autolab PGSTAT 204, The Netherlands). The current range was fixed from 10 mA to 10 nA, and PEC measurements were obtained using NOVA software.

3. RESULTS AND DISCUSSION

3.1. Influence of H_2O_2 Content

The electrochemical anodisation method was used to produce highly ordered bundle-free TiO_2 nanotube array films. The influences of H_2O_2 addition, anodisation time, anodisation potential and F content of the ethylene glycol electrolyte on the surface morphology of the oxide layer were evaluated in detail. The top-surface morphologies of Ti foils anodised with different weight percentages of H_2O_2 and cross-sectional views of the oxides are presented in Figure 2 and the corresponding insets, respectively. All of the data, including pore size diameter, tube length, wall thickness, AR and G, of the resultant anodic TiO_2 nanoarchitectures are summarised in Table I. AR and G are calculated as follows:

$$AR = L/(D+2w)$$

$$G = [4\pi L(D+w)]/[(\sqrt{3})(D+2w)^2]+1$$

where L = tube length in nm; D = pore size diameter; w = wall thickness.

As shown in Figure 2, the top-view appearance of the resultant anodic TiO_2 nanoarchitectures is strongly dependent on the weight percentage of H_2O_2. Nanotubes measuring 800 nm in length were obtained in the sample anodised in 1 wt% H_2O_2. The arrays were bundled at the top layer of the nanotubes and caused pore blockage. When 2 wt% H_2O_2 was applied, incomplete nanotubes were formed, and the nanotubular layer slightly increased to 1.1 μm. When 3 wt% H_2O_2 was applied, nanotubes with enlarged diameters (approximately 50 nm) and a length of 1.9 μm were obtained. The external layer covering the nanotubes was minimised, and random interconnected pits began to grow. Interestingly, the diameter of the resultant tubular structures increased to 64 nm and their lengths grew to 2.3 μm when the H_2O_2 content was raised to 4 wt%. At 5 wt% H_2O_2, circular tubular structures with an average diameter of 76 nm and length of 5.6 μm were formed. The pH of the electrolyte in this particular is 6.5, which is near-neutral in comparison with the pH of the electrolytes incorporating <5 wt% H_2O_2. However, the circular tubular structures were damaged, and irregular porous layers of ~0.8 μm thickness emerged when the H_2O_2 content was raised to 10 wt% (Fig. 2(f)). When additional H_2O_2 is added to the electrolyte mixture, the pH of the electrolyte slightly decreases to 6.2 because of H^+ formation.

To obtain a high AR for the nanotube arrays, H_2O_2, a known powerful oxidant, was added to the electrolyte to act as an oxygen provider. At ambient conditions, H_2O_2 is unstable and decomposes to HO_2^- and H^+ (Eq. (1)), which then react to form $^{\cdot}OH$ and $HO_2^{\cdot}$ radicals (Eqs. (1)–(3)). These radicals increase the oxidation rate of the anodisation process (Eqs. (4) and (5)). Field-assisted and chemical dissolution are improved by $^{\cdot}OH$ and $HO_2^{\cdot}$ radicals during the anodisation process. Hence, the growth of strong and bundle-free nanotubes on the Ti substrate was observed with increasing H_2O_2 content in the electrolyte.[17]

In an anodisation process, O^{2-} ions initially migrate towards the Ti-induced growth of passivation layer with a high electric field across the thin layer. This high electric field further induces electric-field dissolution and forms random pits along with the breakdown of the passivation layer. The formation of random pits through electric-field dissolution on the oxide surface in the present study is assisted by polarisation of the Ti–O bond. F^- in the electrolyte serves as an etchant, reacting with the random pits

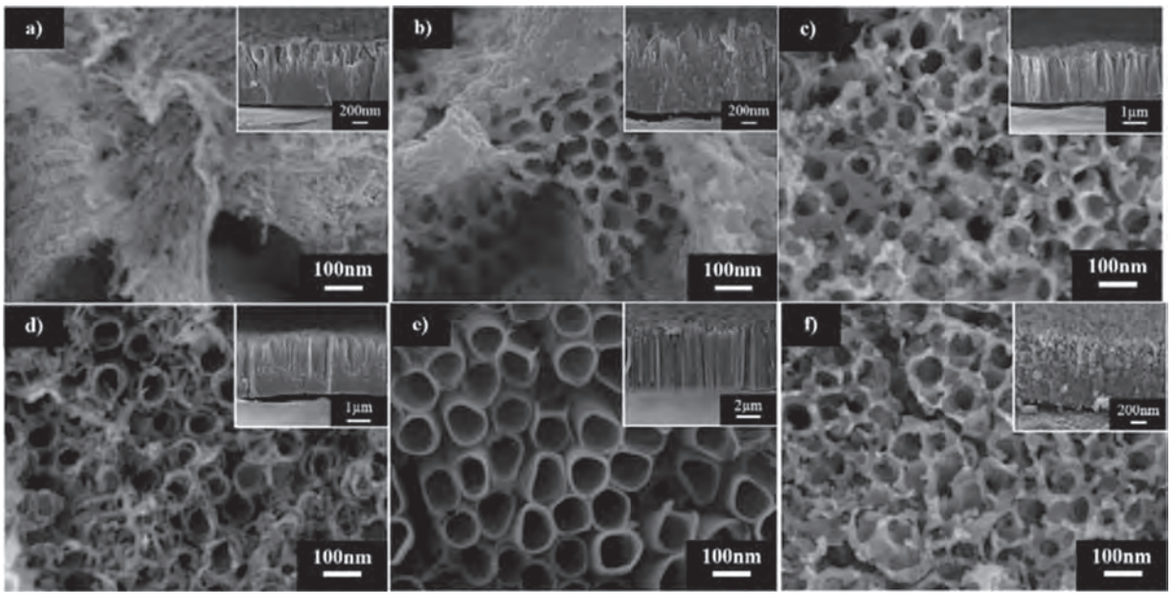

Figure 2. FESEM images of TiO_2 nanoarchitectures obtained under varying H_2O_2 contents in an electrolyte composed of 0.3 wt% NH_4F at 40 V for 60 min: (a) 1 wt%, (b) 2 wt%, (c) 3 wt%, (d) 4 wt%, (e) 5 wt% and (f) 10 wt%. The inset in each subfigure shows the side views of the samples.

to induce their growth into pores via the formation of the $[TiF_6]^{2-}$ complex (Eq. (6)).[18] The optimal amount of H_2O_2 leads to a high growth rate of self-ordered nanotubular structures. Further increases in H_2O_2 are detrimental to the system, as excessive H_2O_2 causes the production of high levels of H^+ in the electrolyte and reduces the pH of the system to 6.2 (Eq. (1)). High chemical dissolution rates also diminish the formation of nanotubular structures (Eq. (6)). Thus, 5 wt% H_2O_2 was considered the optimal amount for forming circular TiO_2 nanotubular structures with lengths of approximately 5.6 μm.

$$H_2O_2 \rightarrow HO_2^- + H^+ \quad (1)$$

$$H_2O_2 + e^- \rightarrow {}^{\cdot}OH + OH^- \quad (2)$$

$$H_2O_2 + {}^{\cdot}OH \rightarrow H_2O + HO_2^{\cdot} \quad (3)$$

$$Ti \rightarrow Ti^{4+} + 4e^- \quad (4)$$

$$Ti^{4+} + 2H_2O \rightarrow TiO_2 + 4H^+ \quad (5)$$

$$TiO_2 + 6F^- + 4H^+ \rightarrow [TiF_6]^{2-} + 2H_2O \quad (6)$$

Table I. Pore diameter, length, wall thickness, aspect ratio, and geometric surface area factor of TiO_2 nanoarchitectures synthesised in electrolytes with different H_2O_2 contents.

H_2O_2 content (wt%)	Diameter (nm)	Length (μm)	Wall thickness (nm)	Aspect ratio, *AR*	Geometric surface area factor, *G* (m^2g^{-1})
1	–	0.8 ± 0.1	–	–	–
2	–	1.1 ± 0.1	–	–	–
3	50 ± 2.3	1.9 ± 0.1	20 ± 1.4	21.1	120.13
4	64 ± 2.6	2.3 ± 0.2	13 ± 1.3	25.5	159.63
5	76 ± 2.4	5.6 ± 0.1	10 ± 0.9	58.3	380.13
10	57 ± 1.4	0.8 ± 0.1	23 ± 1.8	7.8	44.77

3.2. Influence of Anodisation Duration

Figure 3 shows FESEM images of the samples anodised for different durations from 10 min to 120 min under constant process parameters in ethylene glycol containing 5 wt% H_2O_2 and 0.3 wt% NH_4F at 40 V. After 10 min of anodisation, the circular nanotubular structure was visible but poorly defined and featured a thickness of 1.2 μm (Fig. 3(a)). Small oxide pits randomly form on the oxide layer due to breakdown of the passivation layer under the action of chemical and field-assisted dissolution at a local point of high energy. After 20 min of anodisation, the observed pits showed further oxidation and localised dissolution to produce an interconnected pore structure. Nanotubes of approximately 46 nm diameter and 2.0 μm thickness emerged (Fig. 3(b)). After 30 and 40 min of anodisation, the anodic oxide layer was composed of nanotubular structures with average diameters of up to 50 and 56 nm and average lengths of 3.2 and 4.1 μm, respectively (Figs. 3(c and d), respectively). Anodisation for 50 min resulted in larger and longer uniform nanotubes (diameter, 74 nm; length, 5.1 μm), as shown in Figure 3(e). In Figure 3(f), the anodic oxide layer formed after 60 min of anodisation was composed of round and isolated nanotubular structures. The average diameter and length of these structures were 77 nm and 5.8 μm, respectively. At 120 min of anodisation, the resultant circular tubular structure showed a decrease in growth rate and revealed a slightly increased length of up to 7.3 μm and average pore size of 84 nm.

Given these results, we can conclude that a high growth rate of anodic nanotubular structures can be achieved within 60 min of anodisation. This result is mainly attributed to the presence of H_2O_2 in the electrolyte.

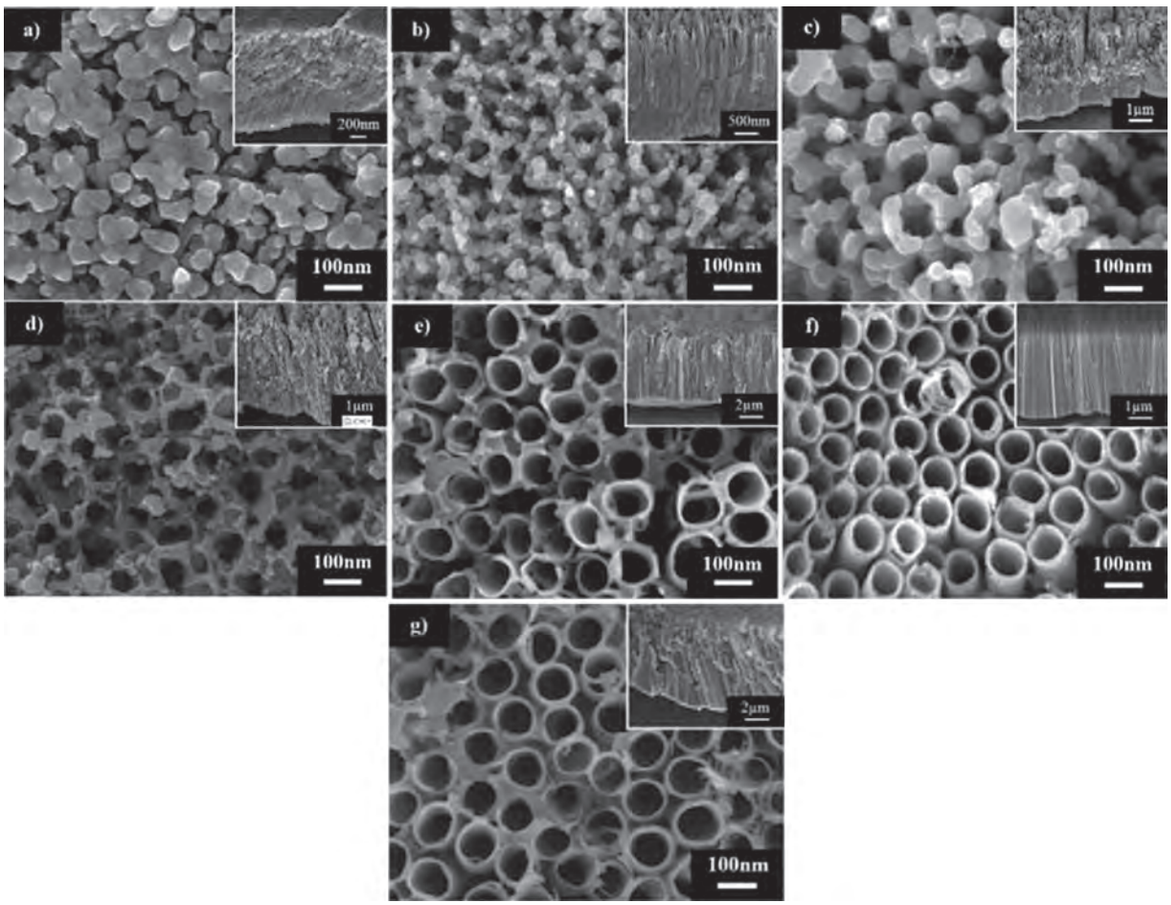

Figure 3. FESEM images of TiO_2 nanoarchitectures obtained under varying anodisation durations in an electrolyte composed of 0.3 wt% NH_4F and 5 wt% of H_2O_2 at 40 V: (a) 10 min, (b) 20 min, (c) 30 min, (d) 40 min, (e) 50 min, (f) 60 min and (g) 120 min. The inset in each subfigure shows the side views of the samples.

As explained in the previous section, the presence of $^{\cdot}OH$ and $HO_2^{\cdot}$ radicals likely triggers high dissolution rates at the bottom of the nanotubes, eventually leading to the production of well-aligned and highly ordered circular tubular structures on the Ti thin films. Indeed, these radicals increased the formation of deep pores and formed high-*AR* and -*G* nanotubes within 60 min of anodisation. After 60 min of anodisation, most of the H_2O_2 is decomposed to form short-lived $^{\cdot}OH$ radicals and consumed in the early stages of the anodisation process.[17,19] Hence, the growth rate of the nanotube arrays decreased. Data related to the resultant anodic TiO_2 nanoarchitectures under different anodisation times are summarised in Table II.

3.3. Influence of Anodisation Voltage

Continuing from the previous portion of the experiment, we fixed the anodisation time and amount of H_2O_2 added to the electrolyte to the optimal process parameters. The anodisation voltage plays a crucial role in controlling field-assisted oxidation and the dissolution rate during electrochemical anodisation. Herein, the applied voltage for anodisation was varied from 10 V to 60 V in fluorinated ethylene glycol with 5 wt% H_2O_2 for 60 min. As shown in Figure 4(a), nanotubes with a diameter of approximately 13 nm and length of approximately 500 nm were successfully produced at a voltage of 10 V. At 20 V, the pore diameter of the circular tubular structures increased up to about 24 nm, and their length grew to about 800 nm (Fig. 4(b)). The Ti foil anodised at 30 V

Table II. Pore diameter, length, wall thickness, aspect ratio and geometric surface area factor of TiO_2 nanoarchitectures synthesised under varying anodisation durations in ethylene glycol containing 5 wt% H_2O_2.

Anodisation duration (min)	Diameter (nm)	Length (μm)	Wall thickness (nm)	Aspect ratio, *AR*	Geometric surface area factor, *G* (m^2g^{-1})
10	–	1.2 ± 0.1	–	–	–
20	46 ± 2.6	2.0 ± 0.1	25 ± 1.5	20.8	112.79
30	50 ± 2.3	3.2 ± 0.1	20 ± 1.8	35.5	201.64
40	56 ± 2.1	4.1 ± 0.2	19 ± 1.4	43.6	253.49
50	74 ± 1.6	5.1 ± 0.1	14 ± 1.2	50.0	313.97
60	77 ± 1.4	5.8 ± 0.2	10 ± 0.9	59.7	390.09
120	83 ± 2.7	7.3 ± 0.1	10 ± 1.3	70.9	465.28

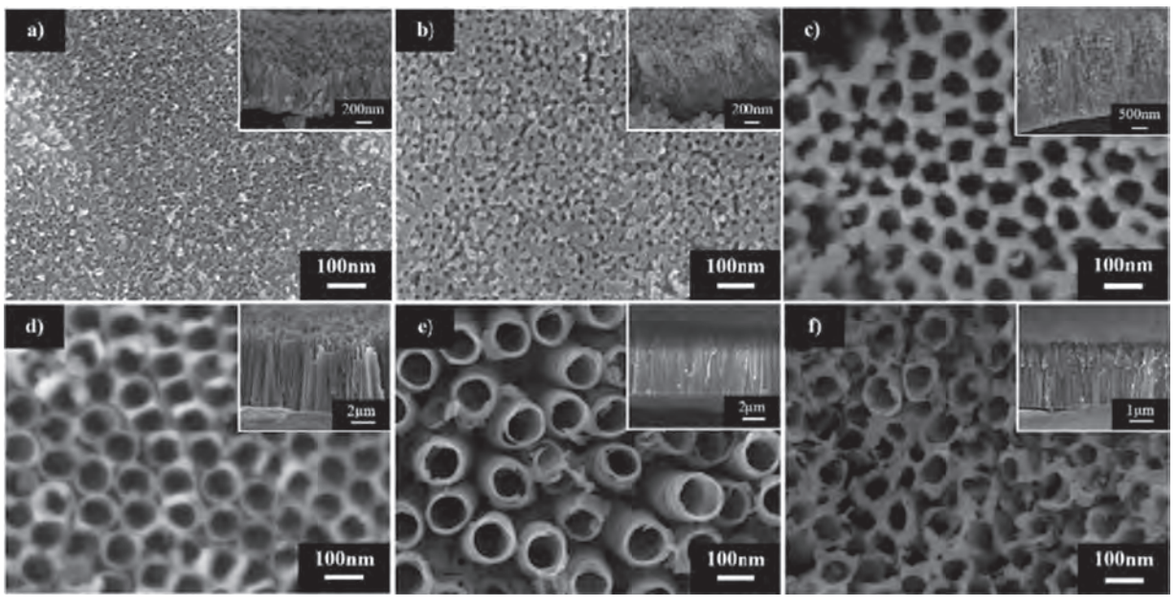

Figure 4. FESEM images of TiO_2 nanoarchitectures obtained under different anodisation voltages in an electrolyte composed of 0.3 wt% NH_4F and 5 wt% H_2O_2 for 60 min: (a) 10 V, (b) 20 V, (c) 30 V, (d) 40 V, (e) 50 V and (f) 60 V. The inset in each subfigure shows side views of the samples.

showed a nanotube diameter and length of up to ~55 nm and 2.5 μm, respectively. Interestingly, when the Ti foil was anodised at 40 V, nanotube arrays with a maximum G (389.11 $m^2 \cdot g^{-1}$) and AR (60.4) and measuring ~74 nm in diameter and 5.8 μm in length (Fig. 4(d)) were obtained. The growth rate of the circular tubular structures decreased remarkably when the applied potential was set to 50 V, forming nanotube arrays with an average diameter of 84 nm and length of ~6 μm (Fig. 4(e)). When a potential of 60 V was applied, short and small tubular structures with a diameter of ~54 nm and length of 3 μm were produced.

The decrease in nanotube size at 60 V may be caused by an imbalance in field-assisted dissolution and oxidation at the anodic oxide layer. A high chemical dissolution rate can etch the top surface of the TiO_2 nanotubes via the formation of a F^- complex (Eq. (6)). High anodisation voltages also provide a large driving force for the etchants H^+ and F^- to promote the chemical dissolution of Ti and TiO_2 (Eq. (6)).[20] The diameter and length of the circular tubular structures are strongly dependent on the applied potential during electrochemical anodisation and closely related to the formation of pits on the oxide layer.[21] Thus, formation of additional pits could be triggered by a high potential through acceleration of the electric field dissolution rate during anodisation. An increased number of pits and further etching produce larger pores under the action of a higher voltage. In this case, pore formation becomes dominant, it was resulting the tubular nanoarchitecture on the anodic oxide layer.[22–23]

At a lower potential, short nanotubes were formed on the Ti foil due to insufficient electric field dissolution during electrochemical anodisation. Further increases in anodisation voltage augmented the nanotube length. This effect may be attributed to the availability of a large driving force for ionic transport through the barrier layer at the bottom of the pores. Hence, faster movement of the Ti/TiO_2 interface into the Ti metal was achieved. The length of the nanotubes further increased until the rate of chemical dissolution of the nanotubes equalled the rates of field-assisted dissolution and oxidation.[3, 10, 13, 24] In the present study, TiO_2 nanotubes with an AR and G of 60.4 and 389.11 $m^2 \cdot g^{-1}$, respectively, were formed in the electrolyte with 5 wt% H_2O_2 under an applied voltage of 40 V over 1 h of anodisation. These conditions favoured the formation of well-aligned and highly ordered TiO_2 nanotubes. Data on the resultant anodic TiO_2 nanoarchitectures obtained under different anodisation voltages are summarised in Table III.

Table III. Pore diameter, length, wall thickness, aspect ratio, and geometric surface area factor of TiO_2 nanoarchitectures synthesised under varying anodisation voltages in ethylene glycol containing 5 wt% H_2O_2 for 60 min.

Anodisation voltage (V)	Diameter (nm)	Length (μm)	Wall thickness (nm)	Aspect ratio, AR	Geometric surface area factor, G ($m^2 \cdot g^{-1}$)
10	13 ± 3.6	0.5 ± 0.1	9 ± 1.0	16.1	84.05
20	24 ± 2.9	0.8 ± 0.1	14 ± 0.9	15.4	82.57
30	55 ± 3.7	2.5 ± 0.1	30 ± 1.2	21.7	117.58
40	74 ± 1.7	5.8 ± 0.2	11 ± 1.5	60.4	389.11
50	84 ± 2.1	6.0 ± 0.2	10 ± 1.4	57.7	379.32
60	54 ± 2.7	3.0 ± 0.1	17 ± 2.3	34.1	200.56

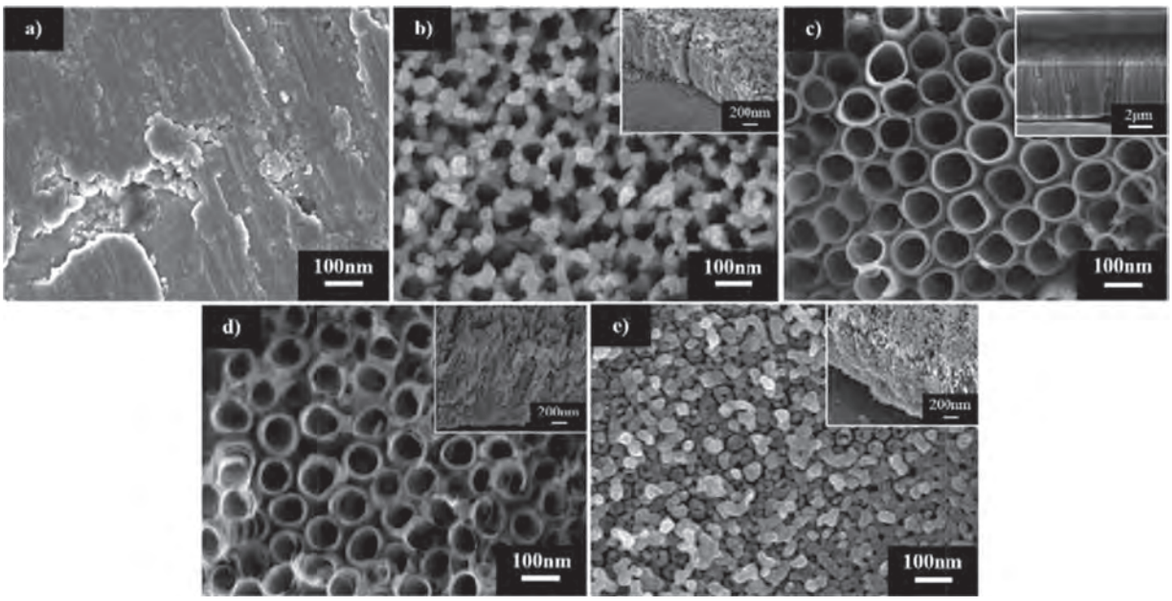

Figure 5. FESEM images of TiO_2 nanoarchitectures obtained under varying F^- contents in electrolyte containing 5 wt% H_2O_2 at 40 V for 60 min: (a) 0.1 wt%, (b) 0.2 wt%, (c) 0.3 wt%, (d) 0.4 wt% and (e) 0.5 wt%. The inset in each subfigure shows side views of the samples.

3.4. Influence of F^- Content

F^- content is known to play a key role in the formation of anodic TiO_2 nanoarchitectures via electrochemical anodisation. Therefore, different amounts of NH_4F in ethylene glycol containing 5 wt% H_2O_2 were investigated. The content of NH_4F was varied from 0.1 wt% to 0.5 wt%, and all samples were anodised at the optimal process parameters (60 min at 40 V) on the basis of the results obtained from the previous portions of the experiment. As shown in Figure 5(a), a thin compact TiO_2 oxide layer was formed on the surface of the Ti foil when 0.1 wt% NH_4F was added to the electrolyte. This result suggests that the amount of F^- in the system was insufficient to accelerate chemical dissolution for pit formation on the anodic oxide layer. When the amount of NH_4F was increased to 0.2 wt%, an irregular nanoporous structure layer with an average diameter and length of 49 and 600 nm, respectively, formed on the Ti foil (Fig. 5(b)). This layer is believed to result from incomplete chemical dissolution at the interface between the Ti-electrolyte interface. With 0.3 wt% NH_4F, a hollow cylindrical oxide with an average diameter of 78 nm and length of 5.5 μm was successfully obtained (Fig. 5(c)). This result indicates that the amount of F^- in the system is sufficient to increase the rate of chemical dissolution and led to further acidification to develop a nanotubular structure. When the NH_4F content was further increased to 0.4 wt%, destructive effects on the resultant anodic oxide layer were observed. The nanotubes were shortened (1.2 μm), and an average diameter of 73 nm was obtained (Fig. 5(d)). Continuous increases in NH_4F content to 0.5 wt% generated smaller pits. Shorter nanotubular structures of approximately 700 nm length were also formed (Fig. 5(e)), which is attributed to excessive chemical etching on the anodic oxide layer in the presence of excess F^-.[25–26] Therefore, the optimal F^- content for the formation of well-aligned and highly ordered nanotubes was determined to be 0.3 wt%. Data on the resultant anodic TiO_2 nanoarchitectures obtained under different NH_4F contents are summarised in Table IV.

3.5. Crystallinity and Phase Analysis

XRD analysis was conducted to determine the compounds existing in the as-prepared and annealed TiO_2 nanotubes. In fact, the as-prepared TiO_2 nanotubes were amorphous in nature.[16] In the present study, heat treatment at 400 °C was conducted to promote crystallisation of TiO_2 from the amorphous phase into the crystalline anatase phase.[15–16] Figure 6 illustrates the XRD patterns of the as-prepared and annealed TiO_2 nanotubes. The presence of anatase and metallic Ti within the TiO_2 nanotubes after heat treatment at 400 °C in air could be noted. The presence of

Table IV. Pore diameter, length, wall thickness, aspect ratio and geometric surface area factor of TiO_2 nanoarchitectures synthesised in electrolyte with 5 wt% H_2O_2 and varying F^- contents at 40 V for 60 min.

Fluoride ion content (wt%)	Diameter (nm)	Length (μm)	Wall thickness (nm)	Aspect ratio, *AR*	Geometric surface area factor, *G* ($m^2 \cdot g^{-1}$)
0.1	–	–	–	–	–
0.2	49 ± 1.6	0.6 ± 0.1	21 ± 2.8	6.6	37.80
0.3	78 ± 2.7	5.5 ± 0.2	10 ± 0.7	56.1	366.63
0.4	73 ± 2.4	1.2 ± 0.1	17 ± 1.9	11.2	64.88
0.5	–	0.7 ± 0.1	–	–	–

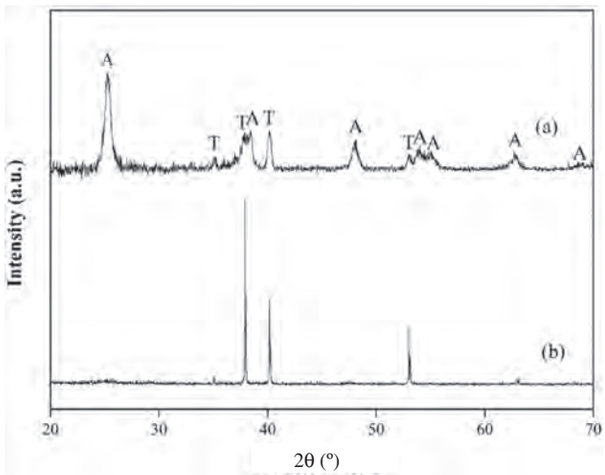

Figure 6. XRD patterns of (a) TiO_2 nanotubes annealed at 400 °C in air and (b) as-prepared TiO_2 nanotubes formed in ethylene glycol with 0.3 wt% NH_4F and 5 wt% H_2O_2 at 40 V for 60 min [T = Ti; A = anatase].

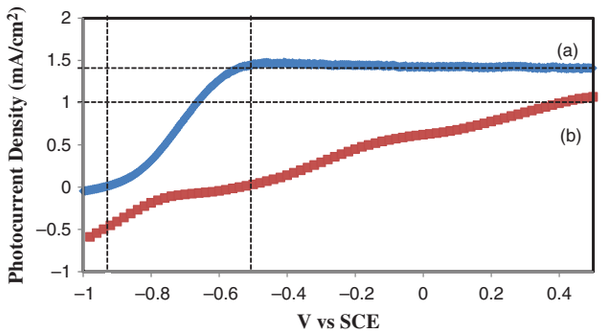

Figure 7. The $j_p - V$ characteristic curves of highly ordered TiO_2 nanotubes with (a) aspect ratio, $AR \approx 56$ and geometric surface area factor, $G \approx 366\ m^2 \cdot g^{-1}$ and (b) $AR \approx 7$ and $G \approx 38\ m^2 \cdot g^{-1}$ obtained from electrolyte with 5 wt% H_2O_2 at 40 V for 60 min. The electrolyte used contained different F^- contents of (a) 0.3 wt% and (b) 0.2 wt%.

anatase TiO_2 was confirmed by diffraction peaks located at 25.37°, 38.67°, 48.21°, 54.10°, 55.26°, 62.66° and 68.74°, which correspond to the (101), (112), (200), (105), (211), (204) and (116) crystal planes, respectively (JCPDS No. 21-1272). The diffraction peaks of the Ti substrate were observed at 35.1°, 38.4°, 40.2° and 53.0°, corresponding to the (100), (002), (101) and (102) crystal planes, respectively. Thus, 400 °C of heat treatment was considered sufficient to convert amorphous TiO_2 into anatase TiO_2, which exhibits thermodynamic stability and increased surface stability for photoelectrochemical activity.[14–15] Given the results, highly crystalline anatase-phase TiO_2 nanotubes were successfully fabricated through electrochemical anodisation and heat treatment at 400 °C.

3.6. Photoelectrochemical Measurements

To gain insights into the correlation between the *AR* and *G* of the anodic TiO_2 and their photoelectrochemical properties, we selected two samples as photoelectrodes to evaluate their responses under illumination. The $j_p - V$ characteristic curves of the selected anodised samples are presented in Figure 7. Interestingly, the photocurrent density of the system was substantially enhanced when the applied voltage was increased from −1 V to 0.5 V under illumination. In particular, TiO_2 nanotubes with $AR \approx 56$ and $G \approx 366\ m^2 \cdot g^{-1}$ exhibited a higher j_p ($1.5\ mA \cdot cm^{-2}$) than TiO_2 nanotubes with $AR \approx 7$ and $G \approx 38\ m^2 \cdot g^{-1}$. The high specific surface area of the nanotubular structure may induce additional light-scattering effects with superior incident light absorption from any direction.[27–28] Hence, additional photo-induced electrons can be released towards the back contact of TiO_2 and eventually shifted to the counter electrode, leading to further reduction of H^+ into hydrogen gas.[29–32] Nanotubes without bundling offer the preferred dimensions for TiO_2 back contact and can improve the transport rate and minimise interfacial recombination of charge carriers considerably.[33–34] In fact, this statement is evidenced by the more-negative photo-potential obtained from sample (a) (−0.9 V) in comparison with that observed from sample (b) (−0.5 V), as presented in Figure 7. A more-negative photo-potential implies a higher electron density on the conduction band of highly ordered TiO_2 nanotubes. These results suggest that the sample with a higher *AR* and *G* also features the highest density of electrons that reach a steady state when no potential and current are applied to the solar-powered photoelectrochemical system. The photocurrent density observed from highly ordered TiO_2 nanotubes without bundling is higher than that observed in other works. In 2016, Zhang et al. reported that sensitised TiO_2 nanotubes can achieve a photocurrent density of $0.87\ mA \cdot cm^{-2}$ under white-light irradiation ($5.9\ mW \cdot cm^{-2}$).[35] Wang et al. and Das et al. reported in 2011 that the use of modified TiO_2 nanotube photoelectrodes yields poor photocurrent density responses ($0.04–0.1\ mA \cdot cm^{-2}$) under a 150 W Xe lamp with monochromatic excitation (λ: 250–600 nm).[36–37] These results may be attributed to their use of samples with a non-uniform pore size (not circular), presence of ridges along the circumference of the nanotubes, and short tube length. Thus, uniform and highly ordered TiO_2 nanotubes function as efficient photoelectrodes with good photoelectrochemical responses. Based on our data, TiO_2 nanotubes with short irregularly serrated surfaces (b) showed poor solar-powered photoelectrochemical responses due to structural disorder and grain boundaries at the oxide layer. These features act as numerous defect and trapping sites. The recombination losses of charge carriers are increased and the photo-induced electrons collected at the TiO_2 back contact are considerably reduced in the presence of porous networks.[38–39] Thus, the j_p of the system incorporating these nanostructures decreased substantially.

4. CONCLUSION

In summary, the optimal electrochemical parameters for the anodisation of Ti foil to form highly ordered and smooth TiO_2 nanotubes with high *AR* and *G* were successfully determined. The optimal processing parameters included 0.3 wt% NH_4F, 5 wt% H_2O_2, 60 min of anodisation and applied potential of 40 V. The anodic TiO_2 nanotubes obtained under these conditions showed superior solar-powered photoelectrochemical performance due to their large specific surface area, which enables enhanced incident photon absorption during illumination.

Acknowledgments: This research work was financially supported by the University Malaya Research Grant (No. RP045B-17AET), University Malaya Research Fund Assistance (BKP) Grant (No. BK096-2016) and Global Collaborative Programme-SATU Joint Research Scheme (No. ST007-2017).

References and Notes

1. J. Jia, L. C. Seitz, J. D. Benck, Y. Huo, Y. Chen, J. W. D. Ng, T. Bilir, J. S. Harris, and T. F. Jaramillo, *Nat. Commun.* 7, 13237 (**2016**).
2. G. Kim, M. Oh, and Y. Park, *Sci. Rep.* 6, 33400 (**2016**).
3. A. Kubacka, M. Fernández-García, and G. Colón, *Chem. Rev.* 112, 1555 (**2011**).
4. C. W. Lai, S. Sreekantan, and Z. Lockman, *J. Nanosci. Nanotechnol.* 12, 4057 (**2012**).
5. F. F. Abdi and S. P. Berglund, *J. Phys. D* 50, 193002 (**2017**).
6. J. M. Macak, H. Tsuchiya, A. Ghicov, K. Yasuda, R. Hahn, S. Bauer, and P. Schmuki, *Curr. Opin. Solid St. M* 11, 3 (**2007**).
7. C. W. Lai and S. Sreekantan, *Micro Nano Lett.* 7, 443 (**2012**).
8. C. W. Lai, S. Sreekantan, and P. S. E., *J. Mater. Res.* 27, 1695 (**2012**).
9. Q. Guo, C. Zhou, Z. Ma, Z. Ren, H. Fan, and X. Yang, *Chem. Soc. Rev.* 45, 3701 (**2016**).
10. J. Zhang, G. Xiao, F. X. Xiao, and B. Liu, *Mater. Chem. Front.* 1, 231 (**2017**).
11. J. Schneider, M. Matsuoka, M. Takeuchi, J. Zhang, Y. Horiuchi, M. Anpo, and D. W. Bahnemann, *Chem. Rev.* 114, 9919 (**2014**).
12. C. W. Lai, J. C. Juan, W. B. Ko, and S. B. Abd. Hamid, *Int. J. Photoenergy* 2014, 524135 (**2014**).
13. Y. C. Nah, I. Paramasivam, and P. Schmuki, *ChemPhysChem.* 11, 2698 (**2010**).
14. C. Ampelli, F. Tavella, C. Genovese, S. Perathoner, M. Favaro, and G. Centi, *J. Energy Chem.* 26, 284 (**2017**).
15. C. W. Lai and S. Sreekantan, *Eur. Phys. J. Appl. Phys.* 59, 20403 (**2012**).
16. T. Luttrell, S. Halpegamage, J. Tao, A. Kramer, E. Sutter, and M. Batzill, *Sci. Rep.* 4, 4043 (**2014**).
17. S. Sreekantan, C. W. Lai, and Z. Lockman, *J. Electrochem. Soc.* 158, C397 (**2011**).
18. C. W. Lai and S. Sreekantan, *J. Nanomater.* 2011, 142463 (**2011**).
19. L. C. Santos, A. L. Poli, C. Cavalheiro, and M. G. Neumann, *J. Braz. Chem. Soc.* 20, 1467 (**2009**).
20. J. Y. Kim, K. Zhu, N. R. Neale, and A. J. Frank, *Nano Converg.* 1, 1 (**2014**).
21. M. Kitano, M. Matsuoka, M. Ueshima, and M. Anpo, *Appl. Catal. A* 325, 1 (**2007**).
22. H. Sopha, L. Hromadko, K. Nechvilova, and J. M. Macak, *J. Electroanal. Chem.* 759, 122 (**2015**).
23. K. Nakata and A. Fujishima, *J. Photochem. Photobiol.* 13, 169 (**2012**).
24. K. Yasuda, J. M. Macak, S. Berger, A. Ghicov, and P. Schmuki, *J. Electrochem. Soc.* 154, C472 (**2007**).
25. S. Ismail, Z. A. Ahmad, A. Berenov, and Z. Lockman, *Corros. Sci.* 53, 1156 (**2011**).
26. L. Trotochaud, T. J. Mills, and S. W. Boettcher, *J. Phys. Chem. Lett.* 4, 931 (**2013**).
27. J. F. Yan and F. Zhou, *J. Mater. Chem.* 21, 9406 (**2011**).
28. T. Jafari, E. Moharreri, A. S. Amin, R. Miao, W. Song, and S. L. Suib, *Molecules* 21, 900 (**2016**).
29. C. W. Lai, K. S. Lau, N. A. Abd Samad, and P. M. Chou, *Curr. Nanosci.* 14, 148 (**2018**).
30. L. D. Sun, S. Zhang, X. W. Sun, and X. D. He, *J. Nanosci. Nanotechnol.* 10, 4551 (**2010**).
31. P. Roy, S. Berger, and P. Schmuki, *Angew. Chem. Int. Ed.* 50, 2904 (**2011**).
32. C. W. Lai and S. Sreekantan, *Nanosci. Nanotechnol. Lett.* 5, 57 (**2013**).
33. Y. Xie, L. Zhou, and J. Lu, *J. Mater. Sci.* 44, 2907 (**2009**).
34. A. Ghicov and P. Schmuki, *Chem. Commun.* 20, 2791 (**2009**).
35. M. Zeng, X. Peng, J. Liao, G. Wang, Y. Li, J. Li, Y. Qin, J. Wilson, A. Song, and S. Lin, *Phys. Chem. Chem. Phys.* 18, 17404 (**2016**).
36. C. Das, I. Paramasivam, N. Liu, and P. Schmuki, *Electrochim. Acta* 56, 10557 (**2011**).
37. J. Wang, Y. Han, M. Feng, J. Chen, X. Li, and S. Zhang, *J. Mater. Sci.* 46, 416 (**2011**).
38. C. Ampelli, F. Tavella, S. Perathoner, and G. Centi, *Chem. Eng. J.* 320, 352 (**2017**).
39. J. F. de Brito, F. Tavella, C. Genovese, C. Ampelli, M. V. B. Zanoni, G. Centi, and S. Perathoner, *Appl. Catal. B* 224, 136 (**2018**).

Received: 28 August 2018. Accepted: 8 November 2018.